View Article Online
View Journal

Green Chemistry

Cutting-edge research for a greener sustainable future

Accepted Manuscript

This article can be cited before page numbers have been issued, to do this please use: G. Matthys, A. Laemont, D. Van Hamme, W. A. Mohamed, L. Bourda, R. Wang, K. Leus, N. De Geyter, R. Morent, R. Lavendomme and P. Van Der Voort, *Green Chem.*, 2026, DOI: 10.1039/D5GC05287D.

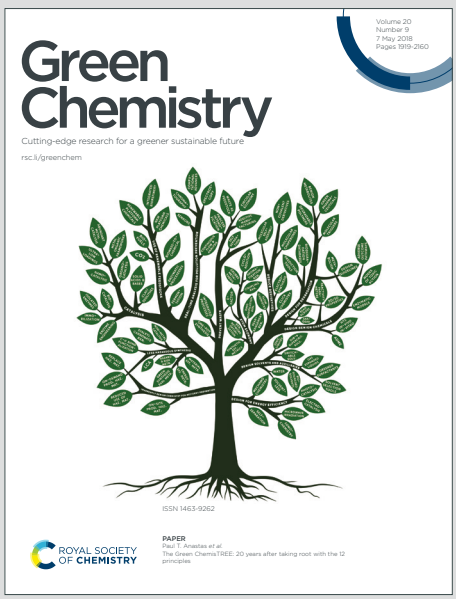

View Article Online
DOI: 10.1039/D5GC05287D

Green foundation box

1. Our work advances green chemistry by replacing hazardous, cyanide-based gold recovery methods with a sustainable "urban mining" solution. We use a robust, recyclable covalent organic framework (COF) that transforms e-waste into a resource.
2. We designed a thiazole-modified COF (Tfpy-PDA-S) that uses light as a clean reductant, eliminating toxic chemicals. This photocatalytic mechanism achieves a record 7980 mg g^{-1} gold capacity and extracts 98% of gold from real-world CPU leachate with high purity (98.35%).
3. The work could be elevated by using bio-based feedstocks, operating with natural sunlight, and developing greener elution processes to close the loop.

Thiazole-Linked Covalent Organic Frameworks for Enhanced Photoreductive Gold Recovery from E-Waste

Gilles Matthys[a], Andreas Laemont[a], Diem Van Hamme[a], Wafaa Ahmed Mohamed[a], Laurens Bourda[a,b], Rundong Wang[a], Karen Leus[c], Natalie De Geyter[c], Rino Morent[c], Roy Lavendomme[d] , Pascal Van Der Voort[a]

[a] Gilles Matthys, Andreas Laemont, Diem Van Hamme, Rundong Wang, Wafaa Ahmed Mohammed, Pascal Van Der Voort
Center for Ordered Materials, Organometallics and Catalysis (COMOC)
Department of Chemistry, Ghent University
Krijgslaan 281- S3, 9000 Ghent, Belgium
E-mail: Pascal.VanDerVoort@UGent.be

[b] Laurens Bourda
Department of Chemistry, KU Leuven
Celestijnenlaan 200 F, 3001 Leuven

[c] Nathalie De Geyter, Rino Morent, Karen Leus
Research Unit Plasma Technology (RUPT)
Department of Applied Physics, Ghent University
Sint-Pietersnieuwstraat 41, B4, 9000 Ghent, Belgium

[d] Roy Lavendomme
Laboratoire de Chimie Organique & Laboratoire de Résonance Magnétique Nucléaire Haute Résolution
Université libre de Bruxelles (ULB)
Avenue F. D. Roosevelt 50, CP160/06-08, B-1050 Brussels, Belgium

Abstract

In this work we developed two different thiazole-linked Covalent Organic Frameworks (COFs) from their imine analogues for the recovery of gold from electronic waste. These gold ions are reduced through a dual-function mechanism: either directly by the COF framework itself or by photocatalytically generated electrons under light irradiation. Two COF systems were investigated: one based on pyrene (Tfpy-PDA) and another on a triazole-triazine core (TTT-TAPB). Initially synthesized with imine linkages, these COFs underwent a post-synthetic modification to convert the imine bonds into more robust thiazole rings. This transformation introduced sulfur atoms, significantly enhancing the gold adsorption performance, recyclability, stability and photophysical properties. Specifically, the thiazole-linked TTT-TAPB-S COF achieved a very high gold adsorption capacity of 3533 mg g^{-1} in dark conditions. Upon light irradiation, the adsorption capacities increased for both imine and thiazole variants, reaching a record high of 7980 mg g^{-1} for the thiazole-linked Tfpy-PDA-S COF. Demonstrating practical utility, these materials effectively removed up to 98% of gold from complex CPU waste leachates with high selectivity and exhibited excellent stability and recyclability.

Introduction

View Article Online
DOI: 10.1039/D5GC05287D

Gold, as a precious metal has held and still holds significant value as a precious metal used in jewelry and finance due to its natural rarity. In more recent years, progress in science and technology has expanded gold's applications beyond these traditional domains.[1] Notably, gold is now widely used in modern technologies such as electronics, nanotechnology, catalysis, sensing, aerospace, and medicine, owing to its exceptional electrical conductivity, malleability, and chemical inertness.[2–7]

The scarcity of gold remains a challenge due to the limited supply from ore mining. However, a significant almost untapped secondary resource of gold exists within discarded electronic devices (e-waste).[8] Traditional pyrometallurgical and hydrometallurgical methods for gold extraction, particularly those employing cyanide pose substantial environmental risks and threats to human health.[9–11] Adsorption offers a greener alternative, but conventional adsorbents are often limited in terms of adsorption capacity, kinetics, and selectivity for gold ions.[12] The urgency for sustainable recovery methods is underscored by the escalating volume of e-waste generated globally, approximately 62 million tons in 2022 with an annual growth rate of 3-5%.[13] Developing efficient and selective techniques for gold recovery from e-waste is crucial from economic and environmental perspectives. Various materials, including ion-exchange resins, activated carbon, porous polymers, and metal-organic frameworks (MOFs), have been developed for gold adsorption.[14–16] However, they often face challenges regarding recovery efficiency, stability, and selectivity in complex waste streams. Consequently, an emerging strategy involves designing selective advanced adsorbents that couple high-capacity sorption with an in-situ reduction mechanism to improve gold recovery.[17]

Covalent Organic Frameworks (COFs) are a promising class of crystalline porous organic materials which are used for applications such as adsorption, (photo/electro) catalysis, sensing, luminescence.[18,19] Their well-defined porous structures, tunable pore sizes, and inherent chemical functionality provide an excellent platform for designing highly selective adsorbents tailored for specific targets like gold ions. For gold recovery, COFs can operate through two primary mechanisms. The first is reductive adsorption, where the electron-rich COF framework itself acts as a solid-state reductant, sacrificially reducing Au(III) to Au(0). The second is photocatalytic reduction, where the semiconducting nature of the COF is harnessed. Under light irradiation, electron-hole pairs are generated, and the photoexcited electrons drive the reduction of Au(III).

However, a significant challenge remains regarding the long-term chemical stability of many COFs, particularly those constructed via reversible imine linkages. These frameworks are prone to structural degradation under the harsh acidic conditions required for electronic waste leaching and subsequent material regeneration, which severely compromises their cycling endurance. Furthermore, many existing imine-linked COFs exhibit a restricted photoresponsive range, hindering the efficiency of light-assisted recovery processes. To address these deficiencies, we investigate a

View Article Online
DOI: 10.1039/D5GC05287D

post-synthetic modification (PSM) strategy that converts less stable imine linkages into robust, sulfur-containing thiazole rings. This transformation is designed to simultaneously enhance the chemical robustness of the framework and introduce soft nitrogen and sulfur active sites with a high inherent affinity for soft $[AuCl_4]^-$ anions, as predicted by Hard-Soft Acid-Base (HSAB) theory.[20–22] By broadening the photophysical response and improving stability in acidic media, this thiazole modification addresses critical gaps in the current state-of-the-art, facilitating a breakthrough in gold recovery performance that is clearly benchmarked against existing materials.[23]

This work systematically designs, synthesizes, and compares two sets of COFs an imine-linked version and its thiazole-linked analogue to evaluate their performance in gold recovery. We aim to elucidate the interplay between the reductive adsorption and photocatalytic mechanisms and demonstrate the practical utility of these materials for selective gold extraction from complex e-waste streams.

Results and Discussion

Synthesis and characterization

We synthesized two distinct covalent organic frameworks (COFs). First, we constructed a pyrene-based imine COF which is popular for its light-harvesting properties, π surface (for π-Au interactions), and ease of synthesis.[24] The polycondensation of 1,3,6,8-tetrakis(p-formylphenyl)pyrene (Tfpy) and p-phenylenediamine (PDA) under the green COF synthesis conditions we developed led to Tfpy-PDA COF (Scheme 1).[25] Another COF based on [1,2,4]-triazolo-[1,3,5]-triazine core was selected due to its planarity and high density of nitrogen sites which are known to coordinate effectively with gold(III).[26] These COFs were made through the polycondensation of 4,4',4"-(tris((1,2,4)triazolo)-(1,3,5)-triazine-tribenzaldehyde (TTT) as an aldehyde linker combined with 1,3,5-tris(4-aminophenyl)benzene (TAPB) which led to TTT-TAPB COF. Subsequently, to enhance the chemical stability of these imine-linked COFs and introduce additional binding sites for gold, we performed a post-synthetic modification using elemental sulfur. This reaction converted the imine linkages into thiazole rings (Scheme 1).

View Article Online
DOI: 10.1039/D5GC05287D

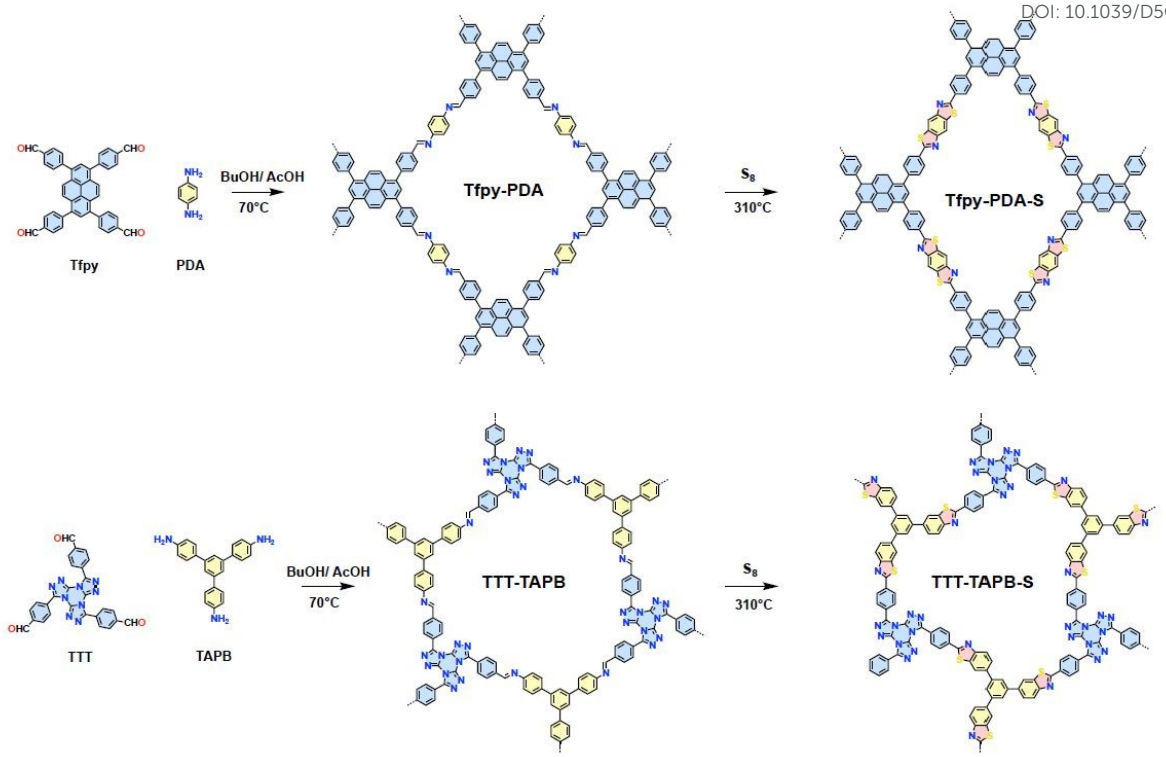

Scheme 1: Synthesis of the imine COFs Tfpy-PDA and TTT-TAPB followed by the post-modification step towards the thiazole COFs Tfpy-PDA-S and TTT-TAPB-S.

Powder X-ray diffraction (PXRD) indicated that Tfpy-PDA COF and TTT-TAPB COF are highly crystalline materials (Figure 1A-D). The tetratopic Tfpy monomer combined with the ditopic PDA monomer results in the formation of a rhombic 2D layered structure (Cmm2 space group). The XRD pattern Tfpy-PDA COF exhibited pronounced peaks at 3.71°, 5.38°, 7.47°, 8.45°, 11.24°, 12.1° and 15.05° which corresponds with its (110), (020), (220), (130), (330), (240), and (440) reflections respectively. The optimized unit cell parameters based on the experimental data were a= 34.25 Å, b= 32.75 Å, c= 4.42 Å , α = β = γ = 90°, for TFPy-PDA COF with residual factors R_{wp}= 7.78 % and R_p = 6.13 %. After the conversion into Tfpy-PDA-S COF, the peaks shifted to 3.90°, 5.55°, 7.70° for the (110), (020), (220) facets, respectively. The shift of the diffraction reflections towards higher values is due to the smaller unit cell of Tfpy-PDA-S-COF. The optimized unit cell parameters based on the experimental data were a = 32.60 Å, b = 33.62 Å, c = 3.68 Å, α = β = γ = 90°, for TFPy-PDA-S COF with residual factors R_{wp}= 6.10 % and R_p = 3.62%.

View Article Online
DOI: 10.1039/D5GC05287D

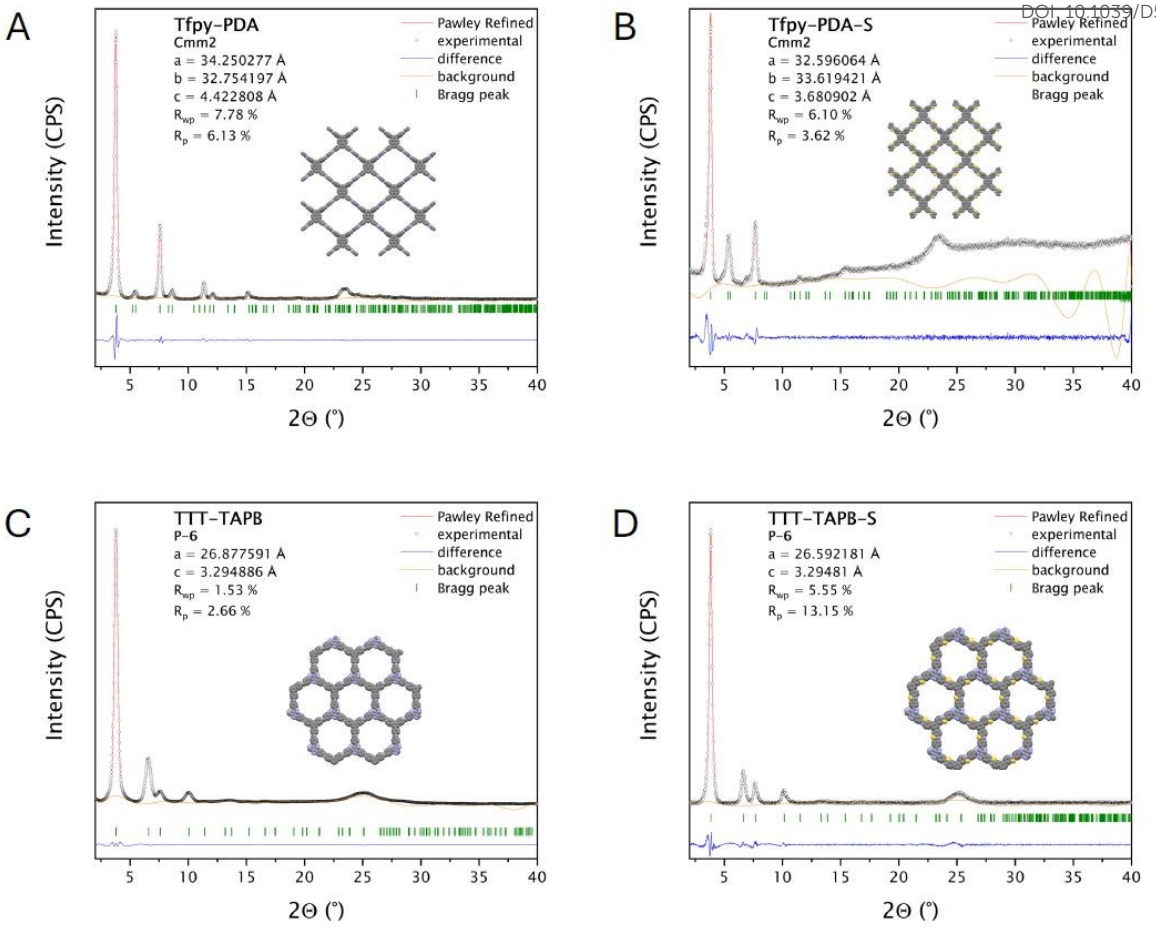

Figure 1: PXRD Pawley refinement of A) Tfpy-PDA, B) Tfpy-PDA-S, C) TTT-TAPB, D) TTT-TAPB-S

The tritopic TTT and TAPB monomers lead to a 2D layered COF structure with hexagonal pores (P-6 space group). The crystalline structure of TTT-TAPB was confirmed with PXRD (Figure 1C). The experimental pattern for TTT-TAPB showed its characteristic reflection peaks at 3.8°, 6.6°, 7.6°, and 10° which corresponds to the (100), (110), (200), and (120), respectively. The experimental data corresponds well with the simulated pattern with AA stacking. The optimized unit cell parameters are a=b= 26.88 Å, c = 3.29 Å and α = β =90°, and γ = 120° with residual factors R_{wp}= 1.53% and R_p = 2.66% . After the post-synthetic modification of the imine-linked TTT-TAPB COF towards the thiazole-linked TTT-TAPB-S COF the crystallinity was investigated by PXRD and confirmed the change in structure. TTT-TAPB-S pattern was highly similar to that of TTT-TAPB COF, and agreed well with the pattern simulated for a thiazole-linked COF with AA stacking. The (100), (110), (200), and (120) peaks shifted slightly to higher 2θ angles: 3.9°, 6.7°, 7.7°, and 10.2°, indicating a small contraction of the unit cell (a = b = 26.59 Å) upon conversion of the imine bond to a five-membered thiazole ring. The residual factors of the Pawley refinement were R_{wp}= 5.55 % and R_p = 13.15%. The Pawley refinement for TTT-TAPB-S yielded an R_p value of 13.15%. This discrepancy is attributed to the harsh, high-temperature (310°C) solid-state synthesis, which likely introduces minor long-range structural defects or disorder not captured by an idealized AA-stacking model. However, the strong visual

View Article Online
DOI: 10.1039/D5GC05287D

match between experimental and simulated patterns (Figure 1D) and the alignment of the (100), (110), (200), and (120) reflections confirm the validity of the assigned framework. The good correspondence between the experimental values of the different COFs and their theoretical models suggested a successful synthesis of these materials. FTIR spectroscopy further confirmed the successful formation of both Tfpy-PDA and TTT-TAPB COFs through the disappearance of characteristic vibrational bands of the aldehyde C=O stretch (around 1700 cm^{-1} for Tfpy and TTT) and the amine N-H stretch (between 3100 – 3500 cm^{-1} for PDA and TAPB). Subsequently, a new stretching vibration corresponding to the imine bond (N=CH) appeared at approximately 1625 cm^{-1} for both COFs (Figure S14). Following the sulfur post-modification the imine stretch vibration disappeared. The formation of the thiazole ring caused a shift of C=N vibration towards 1610 cm^{-1}, although this shift was less discernible for TTT-TAPB due to overlapping vibrations within its triazolo-triazine core (Figure 2A,B). The appearance of new peaks around 1380 cm^{-1} and 815 cm^{-1} in the FTIR spectra of the post-modified COFs (Tfpy-PDA-S and TTT-TAPB-S) are assigned to the C-S stretching and breathing vibrations of the thiazole ring, respectively, strongly suggesting their successful formation. Nitrogen sorption analysis was performed at 77 K to evaluate the porosity of all COFs (Figure 2C,D). The Brunauer-Emmet-Teller (BET) surface area of Tfpy-PDA is 2155 m^2/g (R^2 = 0.999 and C = 170), which after post-modification to TFPy-PDA-S COF reduces to 1295 m^2/g (R^2=0.998 and C = 523). For TTT-TAPB and TTT-TAPB-S the BET surface areas were calculated to be 1384 m^2/g (R^2 = 0.996 and C = 111) and 1124 m^2/g (R^2 = 0.998 and C = 54), respectively (Figure S7). Regarding the shape of the nitrogen sorption isotherms, Tfpy-PDA COF exhibits a type-IV isotherm which corresponds to a mesoporous type of material whilst Tfpy-PDA-S COF has a type-I isotherm which is characteristic of microporous materials (pore size < 2 nm). TTT-TAPB COF and TTT-TAPB-S COF both show Type-IV isotherms coherent with their mesoporous pore size (> 2 nm). After the post-modification step, pore size analysis with quenched-solid density functional theory (QSDFT) (using the cylindrical/sphere pore, adsorption branch kernel) also shows a reduction in pore sizes (Figure S8). Due to the cyclization of the imine linkage in Tfpy-PDA COF into a thiazole linkage in Tfpy-PDA-S, the pore contracts, leading to a decrease in pore size from 2.19 nm to 1.98 nm. This can also be observed for the conversion of TTT-TAPB COF into TTT-TAPB-S COF where the pore sizes are 2.31 nm and 2.18 nm, respectively.

View Article Online
DOI: 10.1039/D5GC05287D

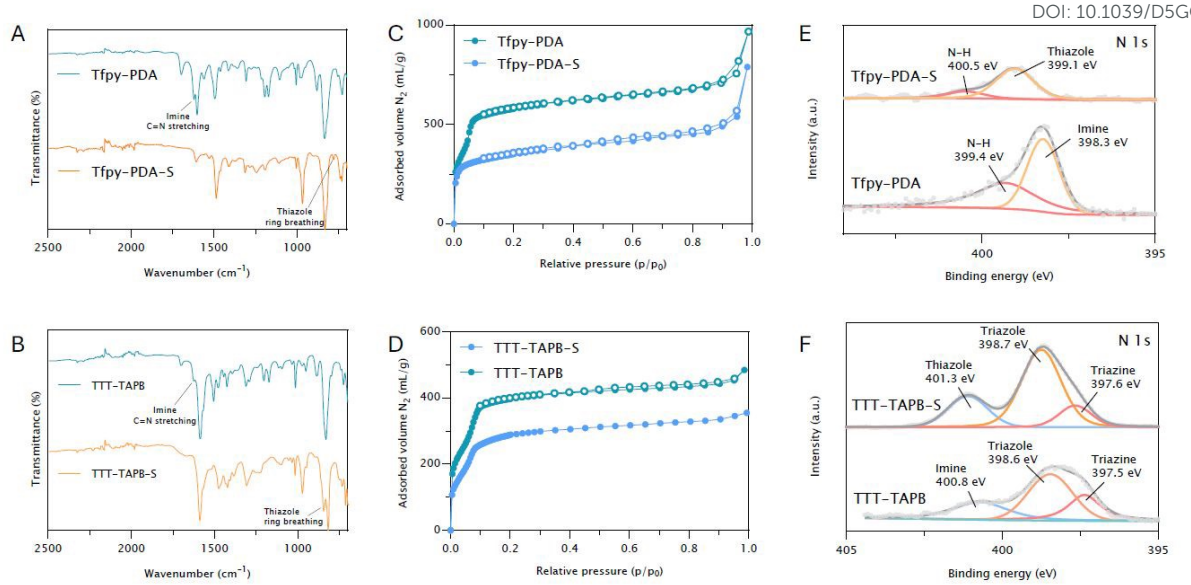

Figure 2: Comparison of Tfpy-PDA and TTT-TAPB before and after post-modification using (A,B) FT-IR spectroscopy, (C,D) nitrogen sorption, and (E,F) nitrogen XPS

X-ray photoelectron spectroscopy (XPS) data (Figure 2E,F) further corroborates the successful conversion of imine linkages towards the thiazole linkages in both COFs. The N 1s spectrum of Tfpy-PDA, the peak at 398.3 eV, assigned to imine nitrogens, shifted to 399.1 eV in Tfpy-PDA-S COF which is indicative of a change in the electronic environment around the nitrogen atom suggesting formation of the thiazole linkage. A similar trend was observed for TTT-TAPB COF, with the imine nitrogen species shifting from 400.8 eV to 401.3 eV. Thermogravimetrical analysis under air further confirmed the thermal stability of these COFs up to temperatures exceeding 200°C (Figure S13). A comparison of chemical stability revealed that upon immersion in 1 M HCl for 24 hours, thiazole COFs preserved their crystallinity. Conversely, imine COFs underwent deterioration, presumably as a result of acidic hydrolysis of the imine bonds (Figure S27).

Gold adsorption study

The synthesized Covalent Organic Frameworks (COFs) were evaluated as potential adsorbents for gold(III) ions from aqueous solutions.

View Article Online
DOI: 10.1039/D5GC05287D

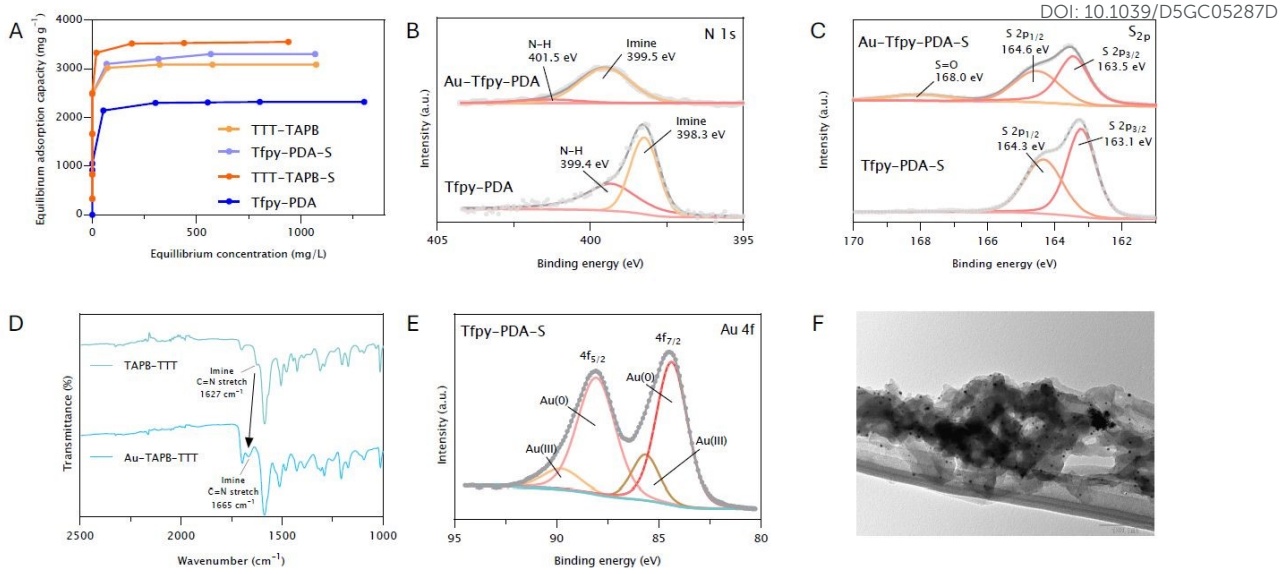

Figure 3: A) Adsorption isotherm of Au(III) in standard dark conditions, B) XPS spectra overlap of N 1s core level of Tfpy-PDA and Au-Tfpy-PDA, C) XPS spectra overlap S 2p core level of Tfpy-PDA and Au-Tfpy-PDA-S, D) FTIR overlap of TTT-TAPB and gold loaded TTT-TAPB, E) XPS spectrum of the Au 4f core level after gold adsorption of Tfpy-PDA-S, F) TEM image of gold adsorbed on Tfpy-PDA

Initial adsorption experiments focused on determining the uptake capacity were performed. Quantitative assessment of the adsorption performance under dark conditions revealed high maximum adsorption capacities (Figure 3A). Tfpy-PDA COF and Tfpy-PDA-S COF exhibits capacities of 2322 mg/g and 3106 mg/g, respectively. The TTT-TAPB COF and its thiazole derivative, TTT-TAPB-S COF, showed even higher capacities of 3088 mg/g and 3533 mg/g, respectively (Table S5).

In the absence of irradiation, the data revealed that gold capture is initially governed by a reductive chemisorption mechanism, wherein the electron-rich COF framework serves as a solid-state reductant. To elucidate the underlying adsorption mechanism and identify the specific active sites, X-ray Photoelectron Spectroscopy (XPS) on both the pristine COFs and the gold-loaded samples were done to evaluate electronic state changes upon gold interaction (Figures S17-18). For the imine-based frameworks, a significant shift of the N 1s core level peak to higher binding energies was observed post-adsorption (Figure 3B). This positive shift of 1.2 eV of the imine species is indicative of a strong interaction between the imine nitrogen and the electron-accepting Au(III) ions, identifying these nitrogen atoms are getting oxidized and act as the primary sites facilitating the initial reduction process.[27] Conversely, for the thiazole-linked COFs, the nitrogen and sulfur atoms both play a role in the adsorption and reduction of gold(III) ions. XPS analysis confirms this, showing that both the N 1s and S 2p core level spectra exhibit a distinct shift after gold adsorption (Figure 3C, S17). Post-adsorption, sulfur XPS on Tfpy-PDA-S and TTT-TAPB-S exhibits as well an oxidized sulfur peak around 168.0 eV , confirming the role as oxidizing species (Figure S18). Complementary insights were obtained from Fourier-Transform Infrared Spectroscopy (FTIR). Changes in the vibrational frequencies of specific functional

View Article Online
DOI: 10.1039/D5GC05287D

groups upon gold adsorption onto the imine COFs corroborated the involvement of nitrogen sites in the interaction (Figure 3D). For Tfpy-PDA COF, the C-N stretching vibration shifted from approximately 1195 cm^{-1} in the pristine material to 1215 cm^{-1} after gold adsorption (Figure S15). For TTT-TAPB COF, the characteristic imine (C=N) stretching vibration experienced a significant shift from approximately 1627 cm^{-1} to 1665 cm^{-1} upon interaction with gold ions (Figure 3D), a similar shift was observed for Tfpy-PDA. These shifts further support the role of nitrogen-containing moieties as key adsorption sites within the imine COF frameworks. For the thiazole COFs no notable shifts were observed probably due to thiazole ring vibrations, which are less discernible in FTIR. Following the initial nucleation at primary N or S active sites in which the COF acts as a stabilizing agent for these gold nanoparticles, a secondary, autocatalytic growth mechanism becomes dominant. Recently, Mishra and co-workers demonstrated that gold nanoparticle seeds can autocatalytically reduce additional Au(III) ions in the dark, a process in which water molecules act as the reductant and are oxidized to hydrogen peroxide (H_2O_2).[28] To verify if this mechanism contributes to the high adsorption capacities in our COF systems, we monitored for H_2O_2 production during gold adsorption in a dark, oxygen-free (argon-purged) environment. Indeed, H_2O_2 was formed during the adsorption experiment, while none was detected in a control experiment without addition of gold(III) salt (Figure S41). After 1 hour, however, no significant further increase in the amount of H_2O_2 was observed which is due to the COF's limited adsorption capacity and growth of the nanoparticles. This finding supports a seed-mediated, autocatalytic growth mechanism, which explains the system's ability to achieve exceptionally high gold loading capacities that far surpass the stoichiometric limits imposed by the initial nucleation sites on the COF framework.

Another important role are electrostatic interactions in the adsorption mechanism. Therefore the surface charge characteristics of the COFs were examined as a function of pH using zeta potential (ζ) measurements (Figure S20). These measurements reflect the net surface charge, which is significantly influenced by the protonation state of nitrogen atoms within the COF frameworks. For all four COFs, the zeta potential transitioned from negative values at higher pH to positive values as the pH decreased. The point of zero charge (pH_{PZC}), where the net surface charge is neutral, was determined to be within the range of pH 5-6 for all materials tested. This finding indicates that within the optimal adsorption range (pH < 6), the COF surfaces possess a net positive charge due to the protonation of accessible nitrogen sites. This positive surface charge facilitates favorable electrostatic attraction with the negatively charged $[AuCl_4]^-$ anions.[29] These results underscore the significant contribution of electrostatic interactions, alongside chemisorption, to the overall gold adsorption process onto these COF materials. Furthermore, examination of the Au 4f core level XPS spectra for all gold-loaded COFs provided definitive evidence of the gold species present (Figures 3E and S19). Deconvolution of the Au 4f signal consistently revealed the presence of gold in two distinct oxidation states: Au(0) and Au(III). Using Tfpy-PDA-S as an example, peaks corresponding to Au(0) $4f_{7/2}$ and $4f_{5/2}$ were identified at approximately 84.4 eV and 88.1 eV, respectively. Concurrently, peaks attributed to

View Article Online
DOI: 10.1039/D5GC05287D

Au(III) $4f_{7/2}$ and $4f_{5/2}$ were observed at approximately 85.6 eV and 89.7 eV. This confirms the coexistence of adsorbed Au(III) ions and reduced elemental Au(0) nanoparticles on the COF surface, validating the reductive adsorption mechanism. Further characterization of the gold-loaded COFs was undertaken to gain insights into the adsorption mechanism and the state of the captured gold. PXRD analysis of the COFs after gold adsorption revealed the emergence of new diffraction peaks at 2θ values of approximately 38°, 44°, 64°, and 78° (Figure S37). These peaks correspond to the (111), (200), (220), and (311) crystallographic planes of face-centered cubic (fcc) elemental gold (Au(0)). This observation strongly indicates together with Au 4f XPS that the major amount of the adsorbed Au(III) ions undergoes reduction to metallic gold nanoparticles during the process. Transmission electron microscopy (TEM) imaging provided direct visual evidence of the formation of gold nanoparticles (AuNPs) within the COF structures after adsorption (Figure 3F & S21-24). These AuNPs were observed to be generally spherical in shape, with sizes ranging from approximately 1 to 20 nm. The presence of these metallic nanoparticles further supports the conclusion that reduction of Au(III) to Au(0) occurs concurrently with adsorption. To further confirm the spatial distribution of the captured gold, Energy-Dispersive X-ray spectroscopy (EDX) mapping was performed. The resulting elemental maps revealed a uniform distribution of gold throughout the COF particles (Figure S25-26).

Upon irradiation with 34 W LED white light, the adsorption capacities were dramatically enhanced (Figure 4A). The capacity of Tfpy-PDA COF increased by 102% to 4680 mg/g, while Tfpy-PDA-S COF showed a 157% increase to 7980 mg/g. Similar enhancements were observed for TTT-TAPB COF (94% increase to 5980 mg/g) and TTT-TAPB-S COF (115% increase to 7620 mg/g). To the best of our knowledge, these values represent some of the highest adsorption capacities reported for gold recovery (Figure 4B). To understand this phenomena we need to investigate the photophysical properties of the COFs. To investigate this a variety of photo-electrochemical characterization techniques were used including Mott-Schottky analysis, electrochemical impedance spectroscopy (EIS), solid state ultraviolet-visible diffuse reflectance spectroscopy (UV-Vis DRS), and photocurrent density chronoamperometry.

View Article Online
DOI: 10.1039/D5GC05287D

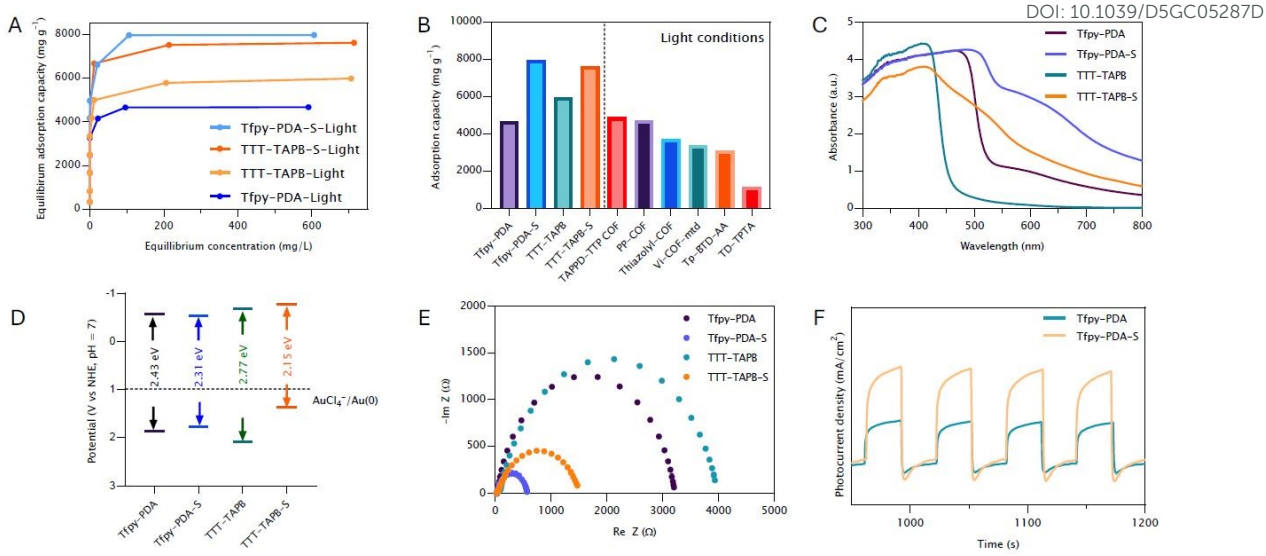

Figure 4: A) Adsorption isotherm of Au(III) upon light irradiation conditions, B) Reported adsorption capacities upon light irradiation, C) Solid-state UV-Vis absorption spectra, D) Band position diagram, E) Electrochemical impedance (EIS) Nyquist plots, F) Photocurrent response curves of Tfpy-PDA and Tfpy-PDA-S.

The system seemingly transitions to a more efficient photo-assisted pathway, leading to an enhanced gold uptake capacity. The prerequisite for this redox reaction is that the Conduction Band Minimum (CBM) of the COF semiconductor must be at a more negative potential than that of the Au(III)/Au(0) couple (+1.002 V vs. NHE). In this pathway, mainly photo-excited electrons in the COF's conduction band drive the reduction of Au(III). To validate this condition, the electronic band structures of the COFs were elucidated via Mott-Schottky analyses (Figure S9). The consistently positive slopes observed in the Mott-Schottky plots for Tfpy-PDA, Tfpy-PDA-S, TTT-TAPB, and TTT-TAPB-S confirm their intrinsic n-type semiconducting nature. The flat band positions (E_{fb}) were determined by the Mott-Shottky curves at different frequencies (1000 Hz, 2000 Hz, and 3000 Hz) at their isoelectric points. The E_{fb} values of Tfpy-PDA, Tfpy-PDA-S, TTT-TAPB, and TTT-TAPB-S were fitted to be -0.56V, -0.53 V, -0.67 V, and -0.77 V vs. NHE (after conversion from SCE), respectively. These values, combined with the optical band gap (E_g) derived from solid-state UV-Vis spectroscopy ($E_{CB} = E_{VB} - E_g$), allowed for the estimation of the valence band potential. As the CBM of an n-type semiconductor is closely approximated by its E_{fb}, these results affirm that the CBM of each COF is substantially more negative than the reduction potential of $[AuCl_4]^-$, thereby providing the necessary thermodynamic driving force for the initial electron transfer (Figure 4D). The precursor imine-linked COFs, Tfpy-PDA COF and TTT-TAPB COF, exhibited optical absorption edges at 536 nm and 460 nm respectively, as determined from UV-Vis DRS (Figure 4C). These values correspond to light absorption primarily in the ultraviolet region, and extending into the visible light. Following post-synthetic modification to the corresponding thiazole-linked COFs (Tfpy-PDA-S and TTT-TAPB-S), a notable broadening of the absorption band towards longer wavelengths was observed. This results in significantly red-shifted absorption edges estimated at approximately 660 nm for Tfpy-PDA-S and 710 nm for

View Article Online
DOI: 10.1039/D5GC05287D

TTT-TAPB-S. This observed bathochromic shift signifies a reduction in the optical band gaps (E_g) for the thiazole-linked COFs compared to their parent imine analogues. This phenomenon is commonly attributed to factors like enhanced π-conjugation facilitated by thiazole moieties compared to imine linkages.[30,31] This optical red shift correlates with structural changes observed in Powder X-ray Diffraction (PXRD) analyses, where shifts to higher diffraction angles suggested a contraction of the unit cell dimensions upon post-modification.

While the favorable conduction band positions of the COFs already confirm the thermodynamic feasibility of gold reduction, electrochemical characterization was employed to probe the difference in charge transfer dynamics of the imine- and thiazole-linked frameworks. Nyquist plots indicated that the thiazole-linked COFs possesses lower charge transfer resistance (R_{ct}) at the material/electrolyte interface compared to their imine-linked counterparts (Figure 4E). This suggests more efficient interfacial charge transfer processes in the thiazole-based systems. Consistent with this finding, photocurrent response measurements under illumination revealed that Tfpy-PDA-S and TTT-TAPB-S generated significantly higher photocurrent densities than Tfpy-PDA COF and TTT-TAPB COF, respectively, indicating enhanced generation and/or separation of photogenerated charge carriers (Figure 4F). The superior charge separation and transfer in the thiazole-based COFs facilitate a more efficient delivery of these electrons to the gold species. This efficient electron transfer, coupled with an autocatalytic effect where the deposited Au(0) nanoparticles themselves serve as catalytic sites to accelerate the reduction of subsequent ions, leads to a faster and more effective gold recovery compared to the imine-linked frameworks. Achieving selective gold recovery from the complex multimetallic matrix of electronic waste is a significant challenge. The observed selectivity for gold(III) can be rationalized by Hard and Soft Acid-Base (HSAB) theory. As a soft Lewis acid, Au(III) exhibits a strong affinity for the COF surface and the (photogenerated) electrons in the conduction band, which act as soft bases. Conversely, competing harder Lewis acids like copper, zinc, and nickel show a weak adsorption interaction, making their photoreduction less favorable.

To further elucidate the initial gold adsorption and reduction mechanism, we employed density functional theory (DFT) calculations at the GGA-PW91 level of theory after geometry optimization for different binding sites on their model compounds, which revealed a synergistic multi-step process. Initially, the $[AuCl_4]^-$ anion is drawn to the framework through a combination of physisorption via Au–Cl···H–C hydrogen bonding and strong electrostatic attraction to the protonated nitrogen sites on the COF. The calculated binding energies for this step highlight a stronger interaction in the parent imine-COFs (4.68–5.09 eV for Tfpy-PDA and 2.71–3.24 eV for TTT-TAPB) compared to their sulfur-modified counterparts (1.38–2.08 eV for Tfpy-PDA-S and 1.71–1.82 eV for TTT-TAPB-S) (Figure S46-49). Following this, a crucial chemisorption step occurs through a ligand exchange where the protonated nitrogen directly binds to the gold center by expelling an HCl molecule to form a covalent N–Au bond; a transformation

View Article Online
DOI: 10.1039/D5GC05287D

that is highly favorable in an aqueous environment due to the strong solvatation and stabilization of the released chloride anion.[32] DFT confirms that all nitrogen sites are energetically favorable anchors for this initial binding of the Au(III) complex, holding it more strongly than sulfur sites by approximately 0.7 eV (Figure 5B,C). After the formation of these covalent Au-N and Au-S bonds, electrons from the conjugated framework can be used to further reduce the Au(III) to Au(0) with a sequential ligand exchange mechanism.[33,34] This pathway involving both nitrogen and sulfur sites are in agreement with the XPS and FTIR observations.

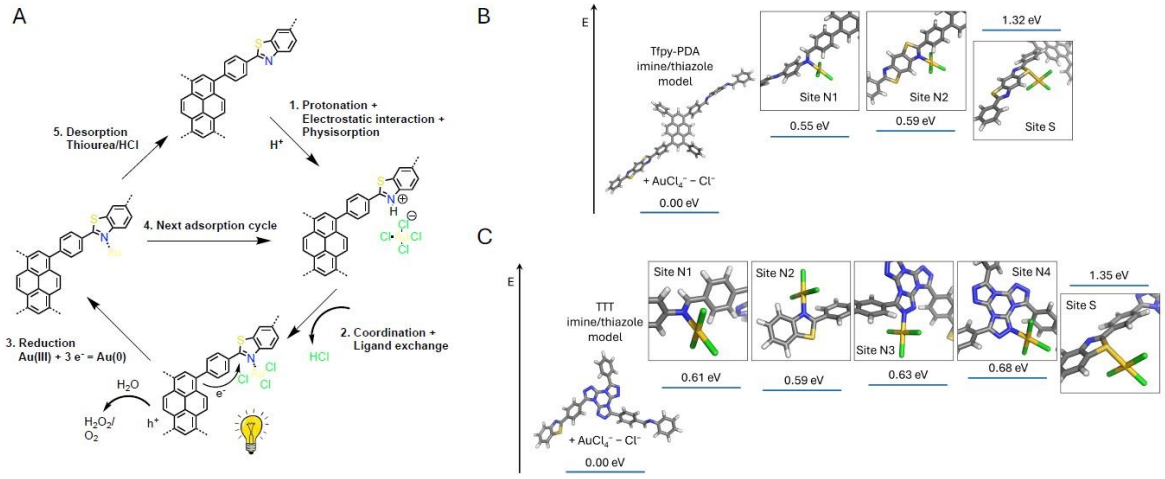

Figure 5: A) Adsorption and photocatalytic redox cycle on nitrogen binding site, Binding energies for chloride ligand exchange on different N and S binding sites for B) Tfpy-PDA and Tfpy-PDA-S model compound , and C) TTT-TAPB and TTT-TAPB-S model compound.

In dark conditions, the coordinated Au(III) complex is relative slowly reduced to metallic Au(0) via direct electron transfer from the electron-rich COF framework. This process gets significantly accelerated under light irradiation, where the COF acts as a photocatalyst. Upon illumination, photoexcited electrons are generated within the framework, providing a powerful and readily available source of reducing agents that rapidly convert the anchored Au(III) complexes to Au(0). We, therefore, propose a mechanism where the abundant nitrogen and sulfur sites first anchor the Au(III) complex, after which the superior photocatalytic properties of the thiazole-COFs facilitate its reduction to metallic Au(0) (Figure 5A). Simultaneously, the corresponding holes (h^+) in the valence band are consumed through the oxidation of water to directly produce hydrogen peroxide (H_2O_2) or oxygen (O_2) which can be further utilized to photosynthesize H_2O_2, thus completing the photocatalytic cycle with water acting as a sacrificial electron donor.[26,35] This could be verified by immersing and irradiating the COF in degassed water which exhibited H_2O_2 productions for each COF in the range between 200-350 µmole after 1 hour (Figure S42).[36] These H_2O_2 values were higher than these determined in dark conditions indicating the system's ability to oxidate water photocatalyticly. Despite this efficient mechanism, the process is ultimately self-limiting due to catalyst passivation. This passivation arises from the system naturally seeking its lowest surface energy state. Nanoparticle growth stops once they reach a

View Article Online
DOI: 10.1039/D5GC05287D

size and shape where it is no longer energetically favorable to get bigger, achieving a stable thermodynamic equilibrium on the COF surface.[37]

Gold Adsorption from Electronic Waste

To evaluate the performance under more demanding, realistic conditions, the practical feasibility of utilizing these COFs for selective gold recovery from electronic waste was assessed using a leachate derived from computer processing unit (CPU) scrap. Such leachates typically contain a complex mixture of metals, presenting a significant challenge for selective extraction. The CPU scrap was first dissolved using an aqua regia leaching solution and afterwards dilluted and adjusted to a pH of 4. Inductively coupled plasma mass spectrometry (ICP-MS) analysis of the resulting leachate revealed the presence of multiple metal ions, primarily copper (385 ppm), nickel (126 ppm), and zinc (9 ppm), alongside a lower concentration of gold (5.9 ppm). Building upon the excellent selectivity observed in synthetic solutions, all four COFs were tested for gold recovery from this complex CPU leachate (Figure 6A,B). High gold removal efficiencies were achieved (without irradiation): Tfpy-PDA COF removed 95% of the gold, while Tfpy-PDA-S COF removed 94%. Similarly, TTT-TAPB COF and TTT-TAPB-S COF extracted 98% and 96% of the available gold, respectively. Crucially, the uptake of the other major metal ions (Cu, Ni, Zn) was minimal, with removal efficiencies remaining below 10% for all COFs, thereby confirming the outstanding selectivity towards gold in a competitive, multi-element environment. Interestingly, light irradiation did not lower the final residual gold concentration in the e-waste solution beyond what was achieved in darkness. This phenomenon can be attributed to the fundamental difference between adsorption capacity and removal efficiency at low concentrations. The photoreduction mechanism primarily enhances the saturations capacity (Q_{max}) of the material by continuously freeing up active sites through the reduction of Au(III) to Au(0) nanoparticles, a process that is critical only when the adsorbent is nearing saturation. However, the initial gold concentration in the CPU leachate was relatively low (5.9 ppm). At this concentration, the abundant nitrogen and sulfur binding sites available on the pristine COF surface are far from saturation, even under dark conditions. Consequently, the high inherent affinity of the COF for gold driven by the strong chemical interaction between the soft Au(III) ions and the soft donor atoms (HSAB theory) is sufficient to achieve near-quantitative removal (95–98%) without the need for photo-assisted regeneration of sites. Additionally, the complex matrix contains high concentrations of transition metals (Cu, Ni) which render the solution highly colored and opaque. This optical screening effect likely attenuates the penetration of light into the solution, further diminishing the contribution of the photocatalytic pathway compared to the clear, simulated solutions.

To complete the recovery cycle and demonstrate the practical feasibility of obtaining high-purity metal, a final recovery step was performed using Tfpy-PDA-S COF. After its saturation with gold from the CPU leachate, the adsorbed metal was eluted from the COF framework using an acidic thiourea solution (thiourea/HCl). The gold in the

View Article Online
DOI: 10.1039/D5GC05287D

resulting eluate was then chemically reduced with sodium metabisulfite ($Na_2S_2O_5$), which precipitated a fine, dark yellow gold powder (Figure 6E). Subsequent analysis of this recovered solid by ICP-MS confirmed a gold purity of 98.35%, a value equivalent to 23.6 karats. This result validates the efficacy of the complete adsorption-desorption-reduction cycle for selective gold capturing from complex electronic waste streams.

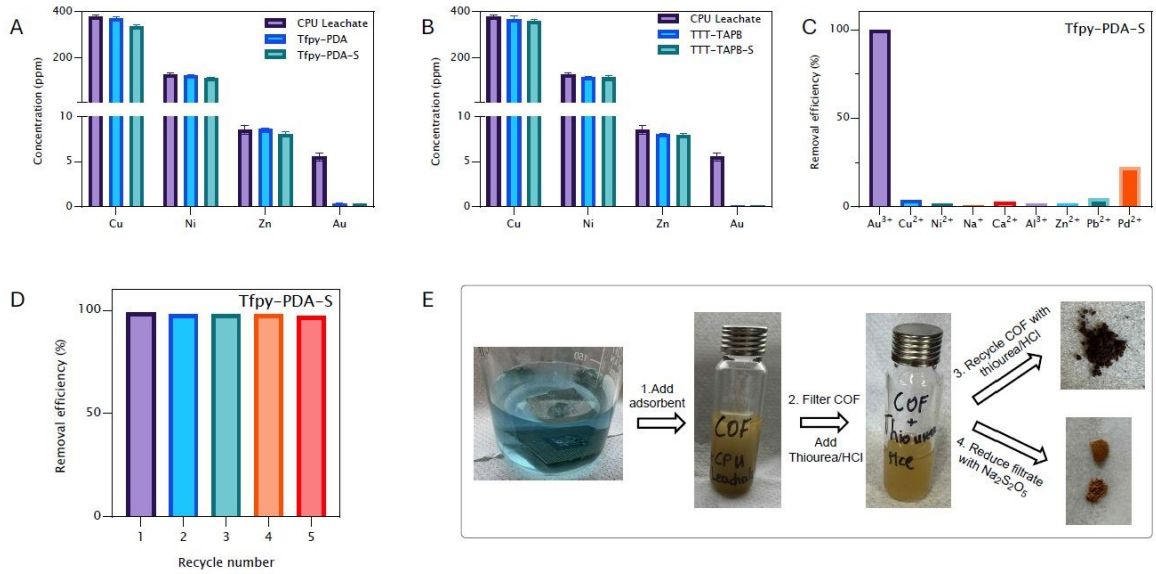

Figure 6: Removal efficiency Au , Cu, Ni, Zn in a CPU leaching solution using A) Tfpy-PDA and Tfpy-PDA-S, B) TTT-TAPB and TTT-TAPB-S, C) Selectivity of Tfpy-PDA-S with common competing ions in e-waste, D) Recyclability of Tfpy-PDA-S for the removal efficiency of a 100 ppm Au(III) solution, E) Practical routine for the recovery of gold from CPU-waste using COFs .

The selective recovery of gold from complex mixtures is critical for practical applications, particularly in electronic waste recycling. Therefore, we added the most commonly encountered ions in e-waste together (Figure 6C & S33). The selectivity of the COFs was assessed using a solution containing 10 ppm of Au(III) alongside several competing metal ions commonly found in such waste streams (e.g., Cu(II), Ni(II), Zn(II), Pd(II), Ca(II), Pb(II)) ,all initially present at 100 ppm. All four COFs demonstrated excellent selectivity for Au(III). The calculated distribution coefficients (K_d) for Au(III) exceeded 33 x 10^4 mL/g for all materials. Conversely, the K_d values for the competing cations remained below 1 x 10^3 mL/g. These results highlight the ability of these COFs to selectively capture gold even in the presence of high concentrations of other metal ions.

The potential for reuse was also examined under light irradiation (Figures 6D and S40). The thiazole-linked COFs exhibited high removal efficiencies over five cycles of adsorption and regeneration. In contrast, the imine-linked COFs showed a gradual decline in performance, attributed to their limited stability in the acidic regeneration solution. Importantly, the characteristic diffraction patterns of the parent COFs were largely retained after desorption of gold, suggesting the preservation of the framework crystallinity throughout the adsorption and subsequent recycling steps (Figure S39).

View Article Online
DOI: 10.1039/D5GC05287D

In contrast to the imine-linked COFs, which showed a gradual decline in removal efficiency after the first adsorption-recycle run. This would be mainly due to the limited stability of imine-linked COFs in an acidic environment, deteriorating the COFs due to hydrolysis of the imine bond (Figure S27, S38).

The kinetics of gold uptake were evaluated using 100 ppm Au(III) aqueous solutions (Figure S30). The parent imine-linked COFs, Tfpy-PDA and TTT-TAPB, demonstrated reasonably fast initial adsorption, achieving removal efficiencies of 82% and 85%, respectively, within the first minute. Complete removal (residual concentration < 1 ppm) was attained after approximately 15 minutes. Notably, the thiazole-linked COFs exhibited accelerated kinetics. Both Tfpy-PDA-S and TTT-TAPB-S achieved remarkable removal efficiencies exceeding 95% within just one minute. Furthermore, these materials reduced the gold concentration to below 1 ppm within 10 minutes, highlighting their rapid uptake capabilities. This kinetic data gave the best fit to a pseudo-second-order model characteristic of processes where electron transfer is the rate-limiting step (Figures S31-S33), which further corroborated the chemisorption mechanism. Water sorption isotherms at 298 K (Figure S52) confirm the hydrophilic nature of all frameworks, a critical requirement for aqueous applications. Notably, the thiazole-linked COFs exhibit sharper water uptake at lower relative humidity compared to their imine analogues. This indicates that the post-synthetic modification enhances surface hydrophilicity, thereby promoting better wettability and facilitating efficient ion transport to the active sites. The influence of solution pH on gold adsorption was investigated, revealing relatively stable adsorption performance across an acidic to neutral range (Figure S34). However, a significant decrease in adsorption capacity was observed at pH values above 7. This reduction is attributed to the base-assisted hydrolysis of the tetrachloroaurate(III) anion, $[AuCl_4]^-$, under alkaline conditions. This hydrolysis leads to the formation of various gold-hydroxo or gold-hydroxo-chloro species, altering the adsorbate's charge and chemical nature, thereby inhibiting effective adsorption onto the COF surface.[38]

Conclusion

In this work, we demonstrate that a simple post-synthetic conversion of imine-linked covalent organic frameworks (COFs) to their thiazole-linked analogues creates highly efficient adsorbents for gold recovery. This modification provides multiple benefits: it enhances chemical stability and recyclability, introduces sulfur binding sites to increase adsorption capacity, maintains high selectivity, and significantly improves the material's photophysical properties. This photophysical enhancement enables a highly efficient photoreduction of gold ions under light, leading to a remarkable maximum adsorption capacity of 7980 mg/g. Critically, these materials demonstrated practical utility by selectively recovering up to 98% of gold from real electronic waste leachates over multiple cycles. Our findings establish this strategy as a straightforward and highly effective route for designing next-generation photocatalytic materials for sustainable resource recovery.

View Article Online
DOI: 10.1039/D5GC05287D

Acknowledgements

G. M. and P.V.D.V. acknowledge the Research Foundation Flanders (FWO-Vlaanderen) (Grant G020521N, Gismo 3G020521). A.L. acknowledges FWO-Vlaanderen (grant 1SB2223N, Gismo 01P07219). R.L. is a Postdoctoral Researcher of the Fonds de la Recherche Scientifique – FNRS and acknowledges Ghent University for a BOF postdoctoral fellowship (Gismo 01P07219). W.A.M. acknowledges the financial support of the Ministry of Higher Education of the Arab Republic of Egypt (Missions Call 2019-2020).

References

1 G. Hutchings, *Nat Chem*, 2009, **1**, 584.

2 L. Qin, G. Zeng, C. Lai, D. Huang, P. Xu, C. Zhang, M. Cheng, X. Liu, S. Liu, B. Li and H. Yi, *Coord Chem Rev*, 2018, **359**, 1–31.

3 A. S. K. Hashmi, *Chem Rev*, 2007, **107**, 3180–3211.

4 S. Witzel, A. S. K. Hashmi and J. Xie, *Chem Rev*, 2021, **121**, 8868–8925.

5 Y. Lu, X. Ma, X. Chang, Z. Liang, L. Lv, M. Shan, Q. Lu, Z. Wen, R. Gust and W. Liu, *Chem Soc Rev*, 2022, **51**, 5518–5556.

6 N. Elahi, M. Kamali and M. H. Baghersad, *Talanta*, 2018, **184**, 537–556.

7 M. M. Ghobashy, S. A. Alkhursani, H. A. Alqahtani, T. K. El-damhougy and M. Madani, *Materials Science and Engineering: B*, 2024, **301**, 117191.

8 P. Peng and A. Shehabi, *Nat Sustain*, 2023, **6**, 93–102.

9 Z. wei Liu, X. yi Guo, Q. hua Tian and L. Zhang, *J Hazard Mater*, 2022, **440**, 129778.

10 Y. Zhang, M. Cui, J. Wang, X. Liu and X. Lyu, *Miner Eng*, 2022, **176**, 107336.

11 A. Akcil, C. Erust, C. S. Gahan, M. Ozgun, M. Sahin and A. Tuncuk, *Waste Management*, 2015, **45**, 258–271.

12 S. Syed, *Hydrometallurgy*, 2012, **115–116**, 30–51.

13 K. Liu, Q. Tan, J. Yu and M. Wang, *Circular Economy*, 2023, **2**, 100028.

14 J. W. Choi, M. H. Song, J. K. Bediako and Y. S. Yun, *Environmental Pollution*, 2020, **266**, 115167.

15 J. Xia, R. Marthi, J. Twinney and A. Ghahreman, *Journal of Industrial and Engineering Chemistry*, 2022, **111**, 35–42.

16 T. Xue, T. He, L. Peng, O. A. Syzgantseva, R. Li, C. Liu, D. T. Sun, G. Xu, R. Qiu and Y. Wang, *Sci Adv*, 2023, **9**, eadg4923.

17 Lady V Quispe-Garrido, J. G. Ruiz-Montoya, A. M. Baena-Moncada and A. La Rosa-Toro, *J Environ Chem Eng*, 2024, **12**, 112585.

18 N. Huang, P. Wang and D. Jiang, *Nat Rev Mater*, 2016, **1**, 16068.

19 L. Bourda, C. Krishnaraj, P. Van Der Voort and K. Van Hecke, *Mater Adv*, 2021, **2**, 2811–2845.

20 S. Xu, M. Richter and X. Feng, *Acc Mater Res*, 2021, **2**, 252–265.

21 Z. Wang, S. Zhang, Y. Chen, Z. Zhang and S. Ma, *Chem Soc Rev*, 2020, **49**, 708–735.

22 N. A. Rejali, M. Dinari and Y. Wang, *Chemical Communications*, 2023, **59**, 11631–11647.

23 Z. Huang, L. Guo, K. Yu, F. Gao, Y. Yang and F. Luo, *Chemical Communications*, 2024, **60**, 4950–4953.

24 F. P. Kinik, A. Ortega-Guerrero, D. Ongari, C. P. Ireland and B. Smit, *Chem Soc Rev*, 2021, **50**, 3143–3177.

25 A. Laemont, G. Matthys, R. Lavendomme and P. Van Der Voort, *Angewandte Chemie International Edition*, 2024, **63**, e202412420.

26 Z. Zhang, Q. Zhang, Y. Hou, J. Li, S. Zhu, H. Xia, H. Yue and X. Liu, *Angewandte Chemie International Edition*, 2024, **63**, e202411546.

27 Z. Li, W. Zhao, C. Li, Y. Yin, D. Wei, Y. Jin, Y. Zhi, J. Qiu, Y. Zhang and J.-B. Baek, *Angewandte Chemie International Edition*, 2025, **64**, e202502199.

28 M. A. Eatoo, N. Wehbe, N. Kharbatia, X. Guo and H. Mishra, *Chem Sci*, 2025, **16**, 1115–1125.

29 A. Zadehnazari, F. Auras, A. A. Altaf, A. Zarei, A. Khosropour, S. Amirjalayer and A. Abbaspourrad, *Nat Commun*, 2024, **15**, 10846.

30 M. Deng, J. Sun, A. Laemont, C. Liu, L. Wang, L. Bourda, J. Chakraborty, K. Van Hecke, R. Morent, N. De Geyter, K. Leus, H. Chen and P. Van Der Voort, *Green Chemistry*, 2023, **25**, 3069–3076.

31 X. Ding, T. Wang, B. Yu, Q. Zhi, H. Wang, H. Liu, P. A. Stuzhin and J. Jiang, *Adv Funct Mater*, 2025, **n/a**, 2422291.

32 B. Đ. Glišić, B. Warżajtis, M. Hoffmann, U. Rychlewska and M. I. Djuran, *RSC Adv*, 2020, **10**, 44481–44493.

33 K. Li, D. Mei, Y. Liu and B. Yan, *Chemistry of Materials*, 2025, **37**, 2535–2545.

34 X. Yang, D. Jiang, Y. Fu, X. Li, G. Liu, X. Ding, B.-H. Han, Q. Xu and G. Zeng, *Small*, 2024, **20**, 2404192.

35 J. Sun, J. Chakraborty, M. Deng, A. Laemont, X. Feng, Y.-Y. Liu and P. Van Der Voort, *J Mater Chem A Mater*, 2023, **11**, 21516–21540.

36 H. Tada, *Nanoscale Adv*, 2019, **1**, 4238–4245.

37 N. T. K. Thanh, N. Maclean and S. Mahiddine, *Chem Rev*, 2014, **114**, 7610–7630.

38 M. Wojnicki, E. Rudnik, M. Luty-Błocho, K. Pacławski and K. Fitzner, *Hydrometallurgy*, 2012, **127–128**, 43–53.

View Article Online
DOI: 10.1039/D5GC05287D

Data Availability Statement

All data generated or analyzed during this study and necessary to support the conclusions are included in this published article and its supplementary information file. The raw data files from the characterization instruments are available from the corresponding author if necessary, Prof. Dr. Pascal Van Der Voort (pascal.vandervoort@ugent.be), upon reasonable request.